# Performance Prediction of Floating Offshore Wind Turbines at Model- and Full-Scale with a RANS method

Álvaro Garrido Vital
ist194809@tecnico.ulisboa.pt
Instituto Superior Técnico, Universidade de Lisboa, Portugal

October 2021

**Abstract**

Floating wind turbines are becoming fashionable within the Renewable Energy world. Numerical analysis is imperative in order to improve the Floating Offshore Wind Turbines designs. This type of wind turbines are affected by both aerodynamic and hydrodynamic loads and modelling the fully coupled response is highly complex. The complete simulation of a full-scale turbine under wind and waves using viscous-flow Computational Fluid Dynamics codes is still nowadays very costly. An alternative is to model the Floating Offshore Wind Turbine behaviour using a scaled turbine of smaller dimensions. One method is using Froude-scaling to model the loads and geometric similarity for the dimensions. However, with this methodology, aerodynamic loads are not scaled properly due to Reynolds dissimilitude that can cause mismatch of it in model- and full-scale turbine. In this work, the aerodynamic analysis of model- and full-scale NREL 5MW wind turbines is performed with a RANS (Reynolds Averaged Navier-Stokes) solver, leaving the hydrodynamic part and coupled analysis for future studies. A different behaviour is determined comparing the performance of both turbines, mainly due to the different Reynolds number that makes the flow fully turbulent at full-scale while for model-scale there is transition. This affects the performance of the model-scale turbine specially at the power coefficient, that drops drastically in comparison with the full-scale one. Focusing on the model-scale turbine, the analysis is made for different grid refinements, turbulence models and transition models performing a verification procedure of the results, obtaining large uncertainties on the power coefficient and mismatch with the experiments, that demonstrate the difficulty of capturing the real flow behaviour with a RANS method.
**Keywords:** Floating wind turbines, RANS, Scale effects, Turbulence models, Transition models

## 1. Introduction

One of the most widespread alternatives for clean and sustainable energy is wind, in substitution to fossil fuels. Onshore wind energy technology has already been used with success in the last decades, with plenty of wind farms deployed worldwide, but it has lots of limitations which constrains the amount of power obtained from the wind such as size limitations, noise reduction or visual impact. During the last years, a next step has been taken with the foundation of bottom-fixed offshore wind installations, that minimize the limitations of onshore wind turbines. Nevertheless, the water depth is a main obstacle for this type of installations so, to avoid that, Floating Offshore Wind Turbines (FOWTs) have been investigated in recent years and, moreover, some installations have been deployed [1, 2]. These turbines are exposed to more loads than the land based ones, such as irregular wave loads, ice loads, collision impact, ocean currents and many others. Modelling the fully coupled aeroelastic and hydrodynamic response is therefore highly complex [3] in order to optimize the FOWTs designs before construction.

In recent years, several numerical studies have been performed to model the aerodynamic behaviour of the wind turbines using computational fluid dynamics (CFD) [4, 5, 6, 7, 8, 9, 10, 11]. Yet the complete simulation of a full-scale free-floating wind turbine under wind and waves using viscous-flow CFD codes is still nowadays very costly.

An alternative is to model the FOWT behaviour using a scaled turbine of smaller dimensions. But to scale the aerodynamic and hydrodynamic behaviour simultaneously is really challenging. A scaling methodology was described and performed on [4] called Froude scaling, a common practice to scale hydrodynamic loads. This methodology consists in maintaining the Froude number $Fr$ of the model- and full-scale turbine the same ($Fr_M = Fr_F$). In this way, the wind speed $V_w$ is determined for the model-scale turbine and the geometry is scaled with a factor $\lambda$.

However, with this methodology, aerodynamic loads are not scaled properly due to the mismatch of the Reynolds number in model- and full-

scale turbine. When a model is Froude scaled, its Reynolds number will be $\lambda^{1.5}$ times smaller than the full-scale Reynolds number. The consequence of this is that the flow at full-scale can be fully turbulent while for the model-scale can be laminar. This difference in the flow behaviour can translate into deterioration of the performance of the model-scale wind turbine with respect to the full-scale one. Therefore, in order to further improve FOWT designs and their model-scale experiments, it is imperative to fully understand in detail the all-scales physics of these turbines.

In this work, a numerical analysis is performed for both model- and full-scale NREL 5MW wind turbine, a turbine designed for FOWTs applications. Aerodynamic analysis will be the focus of the work, leaving the hydrodynamic part and coupled analysis for future studies. A RANS solver will be used on the analysis and special attention will be payed to the accuracy of the results changing the numerical settings (different grid refinements, turbulence and transition models) and performing a verification procedure.

The paper is structured as follows. In Section 2 the geometry and flow conditions for model-scale and full-scale turbine will be presented. Afterwards, the CFD solver ReFRESCO, the computational settings, as well as the applied verification procedure are presented in Section 3. In Section 4, the main results obtained will be presented and discussed while on Section 5 a summary and conclusion will be given.

## 2. Geometry, flow conditions and coordinate system

On **Table 1** the more relevant geometry and performance parameters for both full-scale and model-scale are presented, where the model-scale is scaled using Froude scaling and geometric similarity, with scaling parameter of $\lambda = 50$.

**Table 1:** Properties of the full-scale and model-scale NREL 5MW baseline wind turbine [12]

| Property | Full-scale | Model-scale | Units |
|---|---|---|---|
| Rated power | 5 | 5.7 | $[MW]/[W]$ |
| Rotor diameter | 126 | 2.52 | $[m]$ |
| Hub diameter | 3 | - | $[m]$ |
| Hub height | 90 | 1.80 | $[m]$ |
| Cut-In Rotor Speed | 6.9 | 48.81 | $[RPM]$ |
| Rated Rotor Speed | 12.1 | 85.6 | $[RPM]$ |
| Cut-In Wind Velocity | 3 | 0.42 | $[m/s]$ |
| Rated Wind Velocity | 11.4 | 1.6 | $[m/s]$ |
| Cut-Out Wind Velocity | 25 | 3.54 | $[m/s]$ |
| Rated Tip Speed | 80 | 11.31 | $[m/s]$ |
| Reynolds no. @ 0.7 Radius | 11.5 $\times 10^6$ | 35.7 $\times 10^3$ | $[-]$ |

About the flow conditions, an inflow wind velocity $V_{wind} = 14.1m/s$ is used for the full-scale wind turbine while an inflow wind velocity $V_{wind} = 2m/s$ is used for the model-scale one following the Froude scaling methodology.

The coordinate system used in this study is a Cartesian coordinate system. The origin of the system is located at the intersection of the rotation axis and the swept plane of the rotor. The x-axis is pointing in the opposite direction to the wind direction, while the z-axis is pointing in the vertical upward direction. Finally, the y-axis is pointing in the horizontal direction resulting in a positive Cartesian coordinate system, as shown in **Figure 1**. In this figure also the wind velocity and the rotational direction of the turbine is indicated by vectors $V_{wind}$ and $\Omega$ respectively.

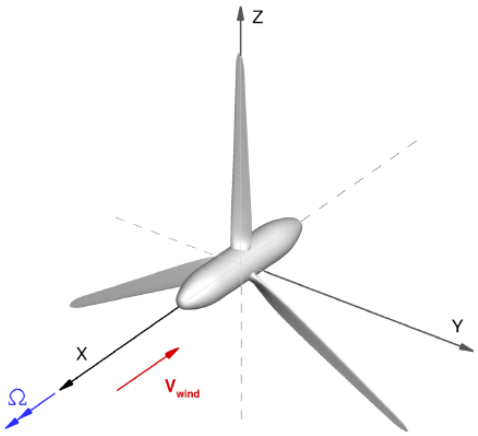


**Figure 1:** Coordinate system for the NREL 5 MW baseline wind turbine [4]

## 3. Numerical tools and settings

### 3.1. CFD solver

The CFD solver called ReFRESCO is used for the numerical analysis of the model- and full-scale wind turbine. ReFRESCO is a viscous-flow CFD code that solves multiphase (unsteady) incompressible flows with the RANS equations, complemented with turbulence models, cavitation models and volume-fraction transport equations for different phases [13]. A finite-volume approach with cell-centered variables is used to discretize the equations with a strong-conservation form and a pressure-correction equation based on the SIMPLE algorithm to ensure mass conservation [14]. First and second order backwards schemes are used for the time integration where at each time step, the non-linear system of the velocity and pressure is linearized using Picard's method, using a coupled or segregated approach. The coupled linear system is then solved with a matrix-free Krylov subspace method using a SIMPLE-type preconditioner. On the other transport equations a segregated approach is always used. The implementation is facebased. Other CFD features as moving, sliding or deforming grids and auto-

matic grid refinement can be used in the code. For turbulence modelling, RANS/URANS, SAS, DES, PANS and LES approaches can be used. To parallelize the code MPI and subdomain decomposition is used, and runs on Linux workstations and HPC clusters. ReFRESCO is currently being developed, verified and validated at MARIN (in the Netherlands) in collaboration wit IST (in Portugal), USP-TPN (in Brasil), TUDelft (in the Netherlands) and UOS (in UK).

In this work, the RANS equations were accompanied with three different turbulence models: Spalart-Allmaras [15], $k-\omega$ SST 2003 [16] and $k-\sqrt{k}L$ [17]. Also a transition model was used, $\gamma - Re_\theta$ [18]. For efficiency and simplicity the turbine tower is neglected.

The rotative motion of the turbine is realized with the AFM method where the RANS equations are solved in the moving reference frame but written in terms of absolute or inertial reference frame quantities. With this method, the flow can be solved, in principle, using steady RANS.

### 3.2. Grid generation

In this study, the grids are generated with *HEXPRESS* [19]. This software generates unstructured hexahedral grids automatically and implements hanging nodes for refinements. This software is really easy to use for the user and the amount of time spent is significantly lower compared to the structured grid generator tools [20].

This also has some disadvantages. The quality of the grid is lower, which implies that a higher number of cells is required to obtain an adequate grid quality. Additionally, the grids generated contain hanging nodes that are usually located on the edges where refinement is implemented. These hanging nodes decrease the quality of the mesh due to additional geometric eccentricity.

All grids are refined toward the geometry of the turbine until a sufficiently refined cell size is obtained at the surface of the turbine blade. Moreover, the grids are refined near the surface of the turbine in order to model properly the viscous layer, based on the dimensionless wall distance $y^+$ to determine the initial cell size at the turbine surface. To properly model the flow near the wall $y^+$ typically needs to be below one.

### 3.3. Domain and boundary conditions

The computational domain consists of a cylindrical volume in which the turbine is placed as shown in **Figure 2**. The total length of the cylindrical domain and its radius are defined as a multiple of the turbine diameter. The origin of the coordinate system and the location of the turbine is at 1/5 the length of the cylinder.

At the inflow boundary A, a uniform inflow velocity and turbulence levels were specified. At the circumferential boundary B, a constant pressure was prescribed, and at the outflow boundary C, outflow boundary conditions (normal gradients equal to zero for all primary variables) were considered. A no-slip condition was applied at the surface of the turbine.

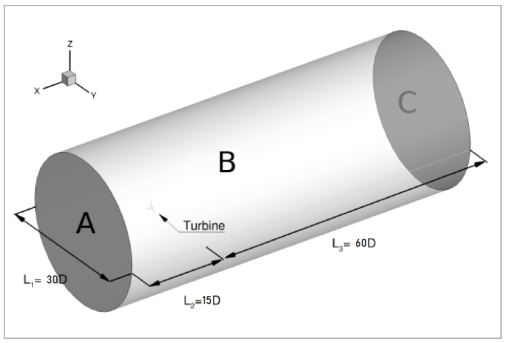


**Figure 2:** Dimensions of the turbine domain [4]

The hub of the turbine is cylindrical shaped with spherically blunted tangent ogive shaped ends, in order to minimize the curvature variation which may induce flow separation. It has a diameter of 200 mm and a length of 1040 mm at model-scale as shown in **Figure 3**.

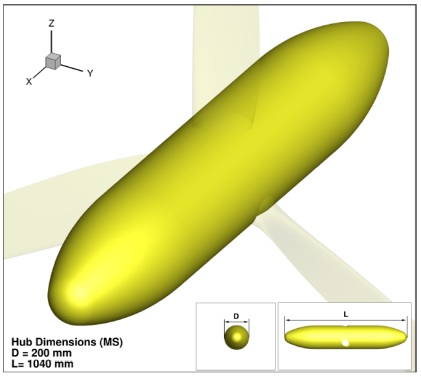


**Figure 3:** Dimensions of the hub at model-scale [4]

### 3.4. Verification

Verification studies determine if the results obtained with the numerical methods are reliable. Verification is a mathematical exercise to verify the code and the solution. The verification procedure that will be described is based on [21]. There are three errors usually present on numerical calculations: round-off, iterative and discretization error.

The round-off error is due to the finite precision of computers. If double or quadruple precision is used, this error can be considered negligible. This error tends to increase with the grid refinement, but in this thesis all the calculations are done with double precision, so it will be considered negligible.

The iterative error is due to the non-linearity of the equations that are solved. For steady flows,

the iterative error can be studied with the convergence history of the simulation. In this study, the $L_2$ and $L_\infty$-norm of the non-dimensional residuals of the flow quantities are used to analyze the iterative error. The $L_2$-norm is defined as $L_2\left(res_\phi\right) = \sqrt{\frac{\sum_{i=1}^{n_p}\left(\left|res_{\phi_i}\right|^2\right)}{n_p}}$ where $res_\phi$ is the non-dimensional change of the residual of a given variable, and $n_p$ the total number of grid cells. The $L_\infty$-norm of the residuals is defined as the maximum absolute change in the whole domain of the residuals of a given variable between iterations.

For the iterative error to be negligible the residuals must be two to three orders below the discretization error, but preferably as low as possible. Also, apart from the convergence residuals, it is determined if the quantities in study, like $C_T$ or $C_P$ are converged sufficiently. The fluctuation of the quantities are monitored for the last 200 iterations and quantified as a percentage of the final iterative value, $U_\phi = 100 \times \max\left(\frac{|\phi_i - \phi_{\text{end}}|}{|\phi_{\text{end}}|}\right)$, where $\phi_i$ is a specific local integral quantity at iteration $i$.The resulting percentage must be at least two to three orders below the discretization uncertainty.

The discretization error usually is the higher order error. It is due to the discretization of the RANS equations to a set of algebraical equations. This error is reduced with grid refinement on steady flows. Doing a refinement study could give insight in the discretization error of the problem. For steady computations, to study the discretization error the numerical uncertainty $U_\phi$ of a solution $\phi_i$ is estimated where the exact solution $\phi_{exact}$ is unknown. The numerical uncertainty for an integral flow quantity $\phi$ is defined by $U_\phi = F_s|\varepsilon|$,where $F_s$ is a safety factor and $\epsilon$ is the estimated discretization error. The discretization error is determined by $\varepsilon \simeq \delta_{RE} = \phi_i - \phi_0 = \alpha h_i^p$, where where $\phi_0$ is the estimate for the exact solution, $\phi_i$ represents any integral of local quantity, $\alpha$ is a constant, $h$ is the typical cell size, and $p$ is the observed order of accuracy.

## 4. Results & discussion

### 4.1. Comparison between Model- and Full-Scale turbines

In this section the RANS computations with ReFRESCO on the full-scale and model-scale NREL 5 MW baseline wind turbine is performed. To scale the wind velocity, Froude-scaling is used as it was discussed before, keeping the geometry the same. An inflow velocity of $V_w = 2m/s$ is used for model-scale conditions while an inflow velocity of $V_w = 14.1m/s$ is used for full-scale conditions. The turbulence model used is the $k-\omega$ SST 2003.

On **Figure 4**, the limiting streamlines for model-scale and full-scale at the suction side of the blade are shown for different TSRs, where TSR is the tip speed ratio. Transition between laminar to turbulent flow can be observed on the model-scale turbine while for the full-scale turbine the flow can be considered fully turbulent as the limiting streamlines are on the airflow direction (no attached flow). Separation occurs at low TSRs only due to heavily loaded blades and large local angles of attack.

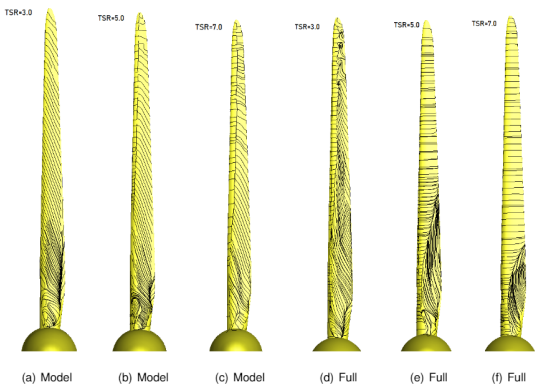


**Figure 4:** Limiting streamlines for model-scale and full scale NREL 5 MW wind turbine at different $TSR$

This difference in the behaviour can be translated in a difference on the performance of the turbines, as can be observed on **Table 2** where this results are also compared with the experimental results at model-scale from [22]. The main difference can be observed on the power coefficient $C_P$, where there is a drastic drop at model-scale in comparison with the full-scale turbine. In addition, there is a mismatch with the experimental results as negative $C_P$ were obtained.

**Table 2:** Power and thrust coefficients for model-scale, full-scale and experiments at different TSRs

| TSR | Model-scale | | Full-scale | | Experiments | |
|---|---|---|---|---|---|---|
| | $C_T$ | $C_P$ | $C_T$ | $C_P$ | $C_T$ | $C_P$ |
| 3 | 0.19 | 0.021 | 0.26 | 0.14 | 0.19 | -0.02 |
| 5 | 0.34 | 0.075 | 0.62 | 0.43 | 0.30 | -0.05 |
| 7 | 0.52 | 0.044 | 0.87 | 0.52 | 0.51 | -0.09 |

### 4.2. NREL 5 MW model-scale at design TSR

This section is focused on the NREL 5 MW model-scale at $TSR = 7$, that it is the design $TSR$ of the turbine. A refinement study will be performed that will follow to a verification procedure, a comparison between three different turbulence models and a transitional model will be used.

#### 4.2.1 Refinement study and verification

In order to determine the numerical uncertainty of the computations, 6 grids are analyzed with the total number of cells varying between $14.3 \cdot 10^6$ and $53.5 \cdot 10^6$. To generate the grids, the initial size of the grids is changed in HEXPRESS as well as the first layer thickness, in order to maintain geometric

similarity as much as possible. The integral quantities $C_T$ and $C_P$ will be used in this analysis.

For the iterative error analysis, grid 3 with $19.6 \cdot 10^6$ cells will be used as a sample. The behaviour of the residuals are similar for all seven grids. On **Table 3** and **Figure 5** the residuals iterative convergence for grid 3 are presented . The $L_2$-norm of the residuals are of order $10^{-4}$, while for the $L_\infty$-norm the order is around $10^{-1}$. A minimum order of $10^{-6}$ and $10^{-3}$ for $L_2$-norm and $L_\infty$-norm respectively is desirable in order to do a verification study. This is not fulfilled in this case. The reason of this could be the unsteady behaviour of the flow at model-scale, specially at the blade root where a vortex is generated as was observed by [23]. The big difference between $L_2$-norm and $L_\infty$-norm also suggests that the residuals are large only locally.

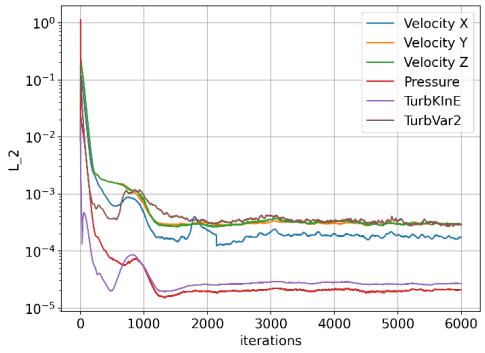


(a)

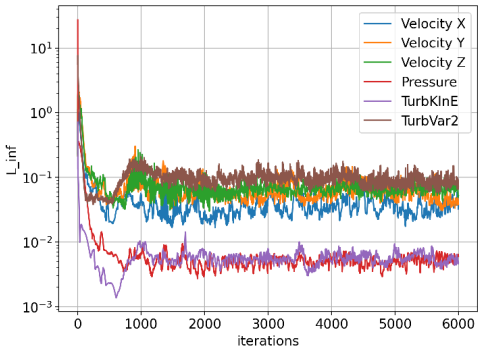


(b)

**Figure 5:** Iterative convergence plots of the $L_2$-norm and $L_\infty$-norm of the residuals for grid 3

The numerical method used is the steady RANS, which could explain the high residuals. Due to the required computational time, unsteady RANS was not considered but it will be desirable at model-scale conditions due to the unsteady behaviour. As can be observed in **Table 3**, the change after the last 200 iterations on the integrals quantities $C_T$ and $C_P$ is below $10^{-3}$ %, which means that despite the large values of the residuals, the integral quantities converge to a constant value. This does not mean that this is the correct value.

In order to be able to neglect the iterative error, the order of convergence must be two to three orders of magnitude below the discretization error. The large iterative error in this case, specially the $L_\infty$-norm, could be too large to be neglected when compared to the discretization error.

The thrust and power coefficients are calculated for the 7 grids in order to determine the discretization error of the computations. In **Table 4** the integral quantities obtained are presented, as well as the numerical uncertainty estimated. As it can be observed, the thrust coefficient and the power coefficient decreases with the number of cells. The power coefficient is more sensitive to the number of cells as it decreases a 62% from the coarsest grid (grid 1) to the most refined grid (grid 7), while for the thrust coefficient the decrease is a 15%. Also, the uncertainty is much higher for $C_P$ than for $C_T$ reaching 350% and 35% respectively. The graphs for the uncertainty estimation are shown in **Figure 6** for grid 7.

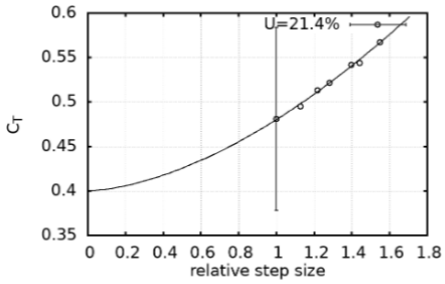


(a)

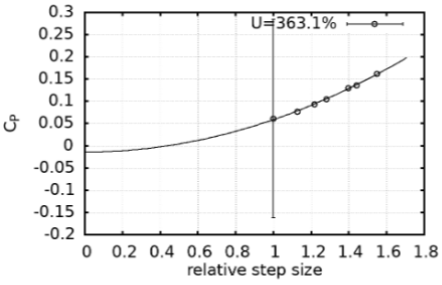


(b)

**Figure 6:** Numerical uncertainty estimation for grid 7

This huge difference between $C_T$ and $C_P$ can be explained with the higher sensitivity to changes in the attached flow region between the computed grids (see **Figure 7**). This is due to the fact that $C_P$ is computed with the moment about the rotating axis of the turbine. As a result of changes in $C_l/C_d$ at the blade tip, $C_P$ is altered significantly

**Table 3:** Iterative convergence and error

| Grid Refinement | max $L_2$ residuals | max $L_\infty$ residuals | Fluc. last 200 iterations $C_T$ [%] | Fluc. last 200 iterations $C_P$ [%] |
|---|---|---|---|---|
| Grid 1 | $5.2 \cdot 10^{-4}$ | $2.8 \cdot 10^{-1}$ | 0.001 | 0.001 |
| Grid 2 | $3.6 \cdot 10^{-4}$ | $4.2 \cdot 10^{-1}$ | 0.001 | 0.001 |
| Grid 3 | $2.2 \cdot 10^{-4}$ | $3.6 \cdot 10^{-1}$ | 0.001 | 0.001 |
| Grid 4 | $1.8 \cdot 10^{-4}$ | $1.7 \cdot 10^{-1}$ | 0.001 | 0.001 |
| Grid 5 | $2.1 \cdot 10^{-4}$ | $2.2 \cdot 10^{-1}$ | 0.001 | 0.001 |
| Grid 6 | $1.7 \cdot 10^{-4}$ | $3.1 \cdot 10^{-1}$ | 0.001 | 0.001 |
| Grid 7 | $1.9 \cdot 10^{-4}$ | $1.5 \cdot 10^{-1}$ | 0.001 | 0.001 |

**Table 4:** Power and thrust coefficients for seven different grids

| Grid Refinement | $C_T$ | $U_\phi$ [%] | $C_P$ | $U_\phi$ [%] |
|---|---|---|---|---|
| Grid 1 | 0.57 | 37 | 0.16 | 356 |
| Grid 2 | 0.54 | 35 | 0.14 | 357 |
| Grid 3 | 0.54 | 33 | 0.13 | 351 |
| Grid 4 | 0.52 | 30 | 0.10 | 345 |
| Grid 5 | 0.51 | 28 | 0.09 | 350 |
| Grid 6 | 0.50 | 26 | 0.08 | 365 |
| Grid 7 | 0.48 | 21 | 0.06 | 363 |

due to the distance from the rotating axis. $C_T$ is computed with the axial thrust force, so changes in $C_l/C_d$ along the blade-span contribute equally. The iterative error could have also affected the uncertainty. Additionally, the fact that $C_P$ has really small values also affects to this uncertainty as a little change represents a large percentage difference.

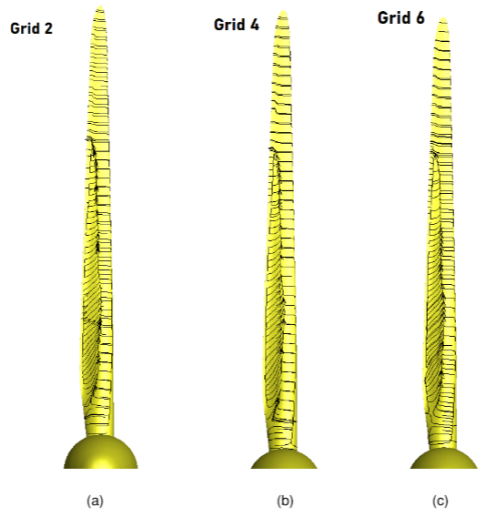


**Figure 7:** Limiting streamlines for different grids

As a conclusion of this study, the challenge of getting appropriate iterative errors using steady calculations for an unsteady flow is observed, which results in large uncertainties especially for the power coefficient. For the following calculations, grid 4 is the one selected taking into account the computational time needed and that it has the lowest uncertainty for $C_P$, the variable more affected in the study.

### 4.2.2 Turbulence modeling

In this section, three different turbulence models are used and compared in order to determine which one is the most suitable to model the flow around the turbine. The models used are the $k-\omega$ SST 2003, Spalart-Allmaras and $k-\sqrt{k}L$.

This three models are compared for a wind speed of $V_{wind} = 2.0$ m/s. The resulting integral quantities $C_T$ and $C_P$ are presented on **Table 5**.

**Table 5:** Power and thrust coefficients for three turbulence models

| Turbulence Model | $C_T$ | $C_P$ |
|---|---|---|
| $k-\omega$ SST 2003 | 0.511 | 0.138 |
| Spalart-Allmaras | 0.655 | 0.286 |
| $k-\sqrt{k}L$ | 0.571 | 0.148 |

In **Figure 8** the limiting streamlines for the suction side are shown for the three turbulence models.

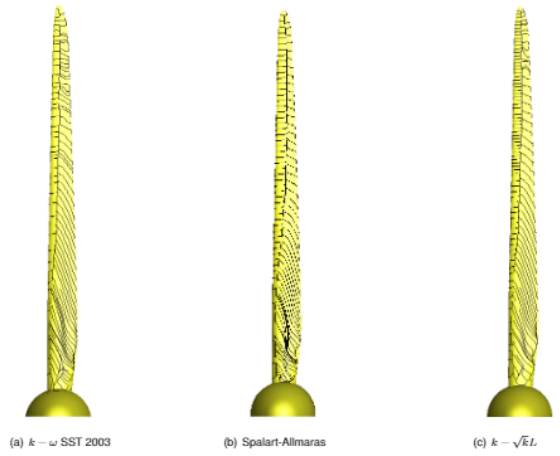


**Figure 8:** Limiting streamlines over the suction side of the turbine blades for three turbulence models

For the three models, the flow in the region near the blade tip remains attached. In this region the apparent angle of attack is much smaller than near the root of the blade and the local velocities are higher. As a result the flow is able to remain attached to the surface.

Near the root, the apparent angle of attack is larger and the flow is not longer able to remain

attached to the blade, which causes the separation and the degradation of the performance of the blade locally. The size of the attached region is significantly smaller for the $k-\omega$ SST 2003 model.

The size of the attached region has direct impact on the power coefficient as, for computing it, the torque around the x-axis is used. In the attached region, the lift generated is higher, so this will contribute significantly to the total moment as it is located near the tip of the blade. This explains the big difference in $C_p$ between the models, where the the Spalart-Allmaras model shows a larger attached flow region and $C_p$ value (**Figure 8**) when compared to the $k-\omega$ SST model and $k-\sqrt{k}L$ model.

The thrust coefficient is computed by the axial force working on the turbine, where lift and drag coefficients over the complete turbine blade span contribute equally, in contrary to the increased contribution of the blade tip with regard to $C_P$ . This leads to a reduction of the sensitivity to the size of the attached flow at the blade tip.

### 4.2.3 Transition model

The $\gamma - Re_\theta$ transition model will be used in order to determine if there is an improvement on the results in comparison with the turbulence models. For the transition model, there is a big influence of the turbulence inlet quantities (eddy viscosity ratio $\frac{\mu_t}{\mu}$ and turbulence intensity $Tu$) on the results of the simulation. The inlet boundary is located 15 diameters upstream from the turbine and a decay of the inlet quantities will occur along the streamwise direction and the values on the turbine will be different from the values at the inlet. To determine which initial values are the ideal ones to model the flow is critical for the simulation. The decay of the turbulence quantities for a uniform flow $U$ are given by the following analytical solutions [24] of the transport equation for $k$ and $\omega$ on the $k-\omega$ SST turbulence model:

$$k = k_{\text{inlet}} \left(1 + \frac{\rho\beta k_{\text{inlet}}}{(\mu_{\text{tinlet}}/\mu)\,\mu U}\,(x - x_{\text{inlet}})\right)^{-\beta^*/\beta},$$
$$\omega = \omega_{\text{inlet}} \left(1 + \frac{\rho\epsilon k_{\text{inlet}}}{(\mu_{\text{tinlet}}/\mu)\,\mu U}\,(x - x_{\text{inlet}})\right)^{-1}, \quad (1)$$

where $k_{inlet}$, $\omega_{inlet}$ and $x_{inlet}$ are the values specified at the inlet. The decay of the eddy viscosity ratio is given by,

$$\frac{\mu_t}{\mu} = \frac{\mu_{\text{tinlet}}}{\mu} \left(1 + \frac{\rho\beta k_{\text{inlet}}}{(\mu_{\text{tinlet}}/\mu)\,\mu U}\,(x - x_{\text{inlet}})\right)^{1-\beta^*/\beta} \quad (2)$$

while the turbulence intensity is directly related with the kinetic energy by,

$$Tu = 100\sqrt{2k/(3U^2)} \quad (3)$$

These equations show a strong decay for the turbulence quantities. In order to control this decay and get realistic values of the turbulence quantities at the turbine, these quantities will be frozen until one radius in front of the turbine. A sensitivity study will be performed in order to determine which is the pair of values more suitable for the simulation.

A sensitivity study changing the values of the initial eddy viscosity ratio will be done. Three cases will be studied for the eddy viscosity: 2, 10 and 50. The turbulence intensity will be set on 10%. On **Figure 9** and **Figure 10** the evolution of the turbulence quantities on the streamwise direction is shown.

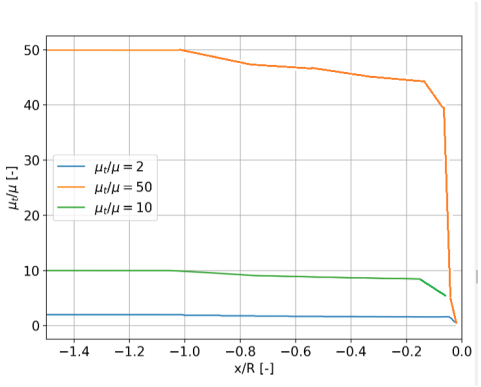


**Figure 9:** Decay of the eddy viscosity ratio along the streamwise direction

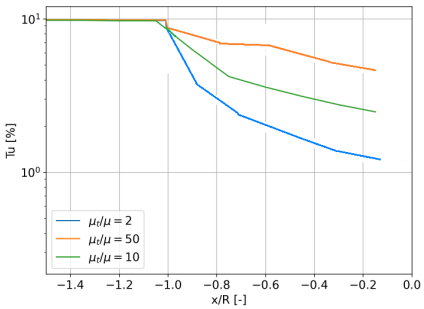


**Figure 10:** Decay of the turbulence intensity along the streamwise direction

A strong decay of the turbulence intensity can be observed on the figure above, while it is less pronounced for the eddy viscosity ratio.

In order to determine if there is a big impact on the results with the eddy viscosity ratio, different parameters will be studied: normalized eddy viscosity contour plots, limiting streamlines, power and thrust coefficients.

On **Figure 11** the normalized eddy viscosity contour plots on different sections of the blade are pre-

sented for the three cases of eddy viscosity ratio studied.

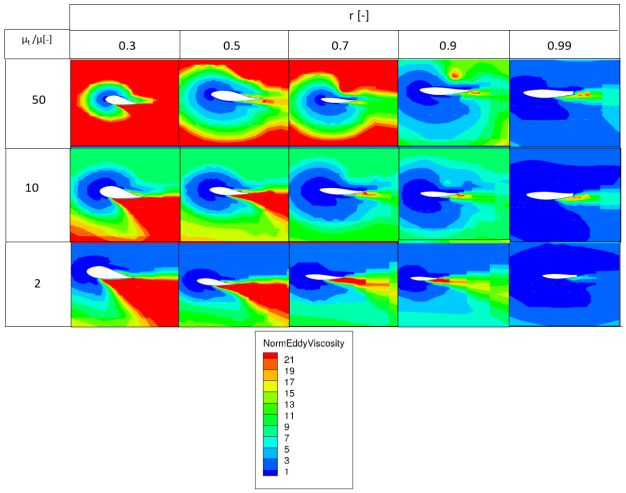


**Figure 11:** Normalized eddy viscosity contour plots on different sections of the blade for the three cases of eddy viscosity ratio

On **Figure 12** the limiting streamlines on the suction side of the blades are presented for the three eddy viscosity ratio cases.

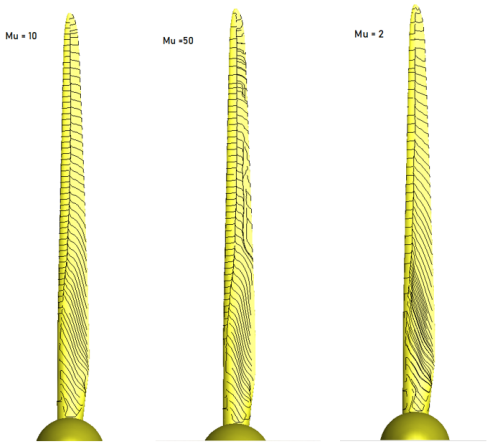


**Figure 12:** Limiting streamlines on the suction side of the blade for the three cases of eddy viscosity ratio

Finally, on **Table 6** and **Figure 13** the thrust and power coefficients are presented comparing them with the results for the turbulence models.

**Table 6:** Power and thrust coefficients for transition and turbulence models turbulence models

| Turbulence Model | $C_T$ | $C_P$ |
|---|---|---|
| $k-\omega$ SST 2003 | 0.511 | 0.138 |
| Spalart-Allmaras | 0.655 | 0.286 |
| $k-\sqrt{k}L$ | 0.571 | 0.148 |
| $\gamma - Re_\theta$ $\mu_t/\mu = 2$ | 0.489 | 0.061 |
| $\gamma - Re_\theta$ $\mu_t/\mu = 10$ | 0.620 | 0.239 |
| $\gamma - Re_\theta$ $\mu_t/\mu = 50$ | 0.683 | 0.319 |

As can be observed on the figures, there are differences between the three eddy viscosity ratio

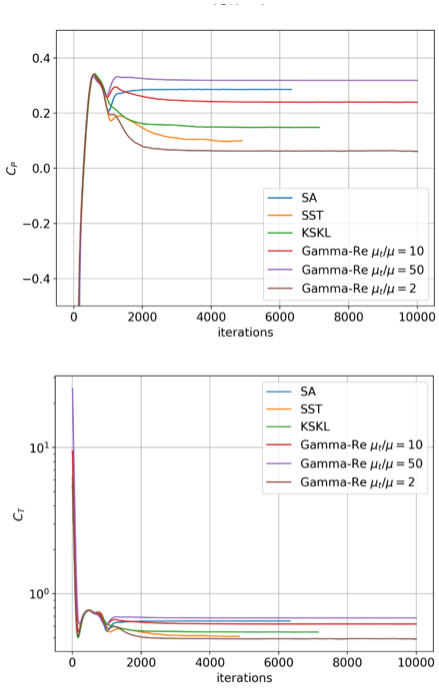


**Figure 13:** Power and thrust coefficients for the transition and turbulence models

cases. As the eddy viscosity increases, the normalized eddy viscosity is bigger around the blade as can be observed on **Figure 11**. Furthermore, as the eddy viscosity ratio increases, the separations occurs before.

About the limiting streamlines (**Figure 12**), a difference in the direction followed by them can be also observed. As the eddy viscosity ratio increases, the number of limiting streamlines on the streamwise direction are higher, which means separation of the flow.

The higher difference between the three cases can be observed on the power and thrust coefficients (**Figure 13**). As the eddy viscosity ratio increases, the power and thrust coefficients increases also. Comparing them with the turbulence models, for eddy viscosity ratio 2, the coefficients are the lowest for all the models while for eddy viscosity ratio 50, the coefficients are the highest. The power coefficient is still positive for the three cases in contrast with the negative results of the experiments.

On **Figure 14** the residuals for turbulence intensity 10% and eddy viscosity ratio 10 are shown in order to observe if there is an improvement with respect to the turbulence models.

As can be observed, there is not an improvement on the residuals and they are even higher than the turbulence models residuals, especially for the

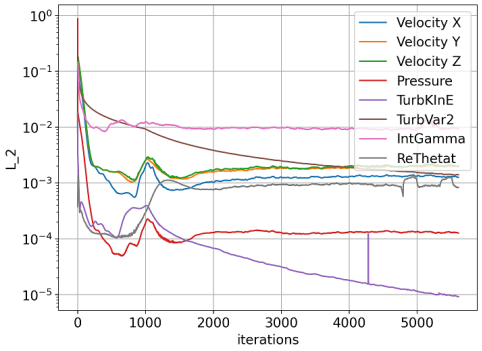


(a)

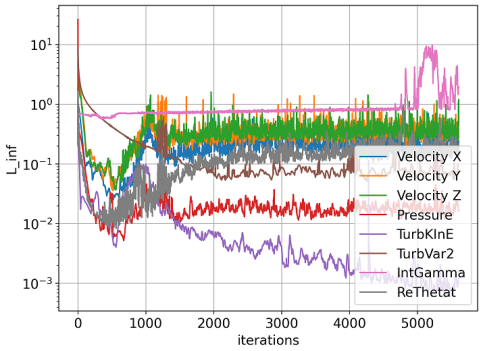


(b)

**Figure 14:** Iterative convergence plots of the $L_2$-norm and $L_\infty$-norm of the residuals for the transition model

variable $\gamma$ of this transition model.

As a conclusion, the transition model has not improved the results of the turbulence models but this does not mean that it is not a good option to model this type of turbine with a transition model. Further studies can be done with the transition model in other to achieve the pair of turbulence quantities that best fits with actual behaviour of the flow.

**5. Conclusions**

First of all, the knowledge obtained from the comparison between the NREL 5MW Wind Turbine at full-scale and model-scale will be summarized:

- The behaviour of the flow around the turbine is different at full-scale and model-scale due to Reynolds dissimilitude that comes from Froude scaling, where aerodynamic forces are not scaled properly. The flow can be considered fully turbulent at full-scale while at model-scale there is transition from laminar to turbulent.

- The different behaviour in the flow causes a poor performance of the NREL 5MW wind turbine at model-scale, specially significant looking at the power coefficient $C_P$, whose value drops drastically for the full-range of TSRs.

The knowledge obtained from the NREL 5MW wind turbine at model-scale will be summarized next:

- Large residuals were obtained with the iterative error study performed on different refined grids. The order of the $L_2$-norm and $L_\infty$ norm residuals obtained was $10^{-4}$ and $10^{-1}$, far from the desirable order, however the integral quantities converged to a constant value. The discretization error obtained was also higher than desirable specially for $C_P$ with uncertainties around 300%, This could be mainly due to the use of a steady RANS at model-scale, where the flow is clearly unsteady.

- Three different turbulence models were used in order to determine which one is the most suitable to model the flow around the turbine at model-scale: $k-\omega$ SST 2003, Spalart-Allmaras and $k-\sqrt{k}L$. Lower values and closer to experimental results for the integral quantities $C_T$ and $C_P$ were obtained for the $k-\omega$ SST model while the higher values were obtained by the Spalart-Allmaras model. This is directly related by the size of the attached region that contributes to the value of the $C_P$. The size of the attached region for the Spalart-Allmaras model is the higher of the three. However neither of the models replicate the behaviour obtained by the experiments for $C_P$, where negative values were obtained.

- The transition model $\gamma - Re_\theta$ was used looking for improvements in the results in comparison with the turbulence models, as transition is presented at model-scale. A sensitivity analysis changing the initial values of the eddy viscosity ratio of the flow was performed. The increase of the the eddy viscosity ratio made the separation to occur closer to the leading edge of the blade. Neither the residuals nor the integral quantities improved in comparison to the turbulence models, as the residuals are still higher than desirable and the $C_P$ values are still positive.

For future studies, an improvement in the scaling methodology of the NREL 5MW wind turbine should be consider in order to obtain a similar aerodynamic behaviour to the full-scale turbine, that will ease the optimization of it.

It is desirable to perform unsteady RANS (URANS) at model-scale, as the flow is highly unsteady. Lower iterative errors and numerical uncertainties are expected when using URANS and it will

give a better understanding of the flow around the turbine.

A deeper study on the transition model could give the ideal pair of initial turbulence quantities that resemble the real flow around the turbine. As at model-scale there is transition, using this type of models is really promising.

Finally, the study of the coupled problems, with the aerodynamic and hydrodynamic loads acting on the turbine will be the last step to properly model FOWTs and help for optimization.

**References**


[1] CleanTechnica. Hywind Scotland, World's First Floating Wind Farm, Performing Better Than Expected, 2018.

[2] OffshoreWIND. WindFloat Atlantic Fully Up and Running, 2020.

[3] J. Jonkman and M. Buhl. Development and Verification of a Fully Coupled Simulator for Offshore Wind Turbines. *45th AIAA Aerospace Sciences Meeting and Exhibit, 8-11 January, Reno, NV, AIAA Meeting Papers on Disc*, 2007.

[4] M. Make and G. Vaz. Analyzing scaling effects on offshore wind turbines using CFD. *Renewable Energy 83*, 2015.

[5] B.Dose et al. Fluid structure coupled computation of the NREL 5MW Wind turbine blade during standstill. 2019.

[6] Jeon M, et al. Unsteady aerodynamics of offshore floating wind turbines in platform pitching motion using vortex lattice method. *Renewable Energy*, 2013.

[7] M. Make, G. Vaz et al. Analysis of aerodynamic performance of floating wind turbines using CFD and BEMT methods. 2015.

[8] S. Lee, M. Churchfield, P. Moriarty, J. Jonkman, and J. Michalakes. Atmospheric and wake turbulence impacts on wind turbine fatigue loading. 2012.

[9] Abdulqadir SA et al. The physical modelling and aerodynamics of turbulent flows around horizontal axis wind turbines. *Energy*, 2016.

[10] N.N. Sorensen et al. Navier–Stokes Predictions of the NREL Phase VI Rotor in the NASA Ames 80 ft x 120 ft Wind Tunnel. *Wind Energy*, 2002.

[11] N.N. Sorensen. CFD Modelling of Laminar-turbulent Transition for Airfoils and Rotors Using the $\gamma - Re_\theta$ Model. *Wind Energy*, 2009.

[12] J. M. Jonkman, S. Butterfield, W. Musial, and G. Scott. Definition of a 5-MW Reference Wind Turbine for Offshore System Development. 2009.

[13] G. Vaz, F. Jaouen, and M. Hoekstra. Free-surface viscous flow computations. Validation of URANS code fresco. *28th International Conference on Ocean, Offshore and Arctic Engineering (OMAE)*, 2009.

[14] C. M. Klaij and C. Vuik. Simple-type preconditioners for cell-centered, colocated finite volume discretization of incompressible reynolds-averaged navier-stokes equations. *International Journal for Numerical Methods in Fluids*, 71(7):830–849, 2013.

[15] S. B. Pope. *Turbulent Flows*, 2000.

[16] F. Menter, M. Kuntz, and R. Langtry. Ten Years of Industrial Experience with the SST Turbulence Model. *Turbulence, heat and mass transfer*, 4, 2003.

[17] F. Menter, Y. Egorov, and D. Rush. Steady and Unsteady Flow Modelling Using the $k - \sqrt{k}L$ Model. *Heat and Mass transfer*, 5, 2006.

[18] R. B. Langtry and F. R. Menter. Correlation-Based Transition Modeling for Unstructured Parallelized Computational Fluid Dynamics Codes. *AIAA Journal*, 47(12), 2009.

[19] NUMECA International. "HEXPRESS Unstructured Full-Hexahedral Meshing.", 2012.

[20] N. International. *HEXPRESS User Manual*, 2017.

[21] L. Eça, G. Vaz, and M. Hoekstra. Verification and Validation Exercise for the Flow over a Backward Facing Step. *European conference on computational fluid dynamics*, 2010.

[22] H. R. Martin. Development of a Scale Model Wind Turbine for Testing of Offshore Floating Wind Turbine Systems. 2011.

[23] E.Ridder et al. Development of a Scaled-Down Floating Wind Turbine for Offshore Basin Testing. 2014.

[24] P. Spalart, C. Rumsey. Effective inflow conditions for turbulence models in aerodynamic calculations. 2007.